nature communications

Article

https://doi.org/10.1038/s41467-026-75373-2

Origin of crack propagation in lithium cobalt oxide positive electrode for lithium-ion batteries

Received: 17 August 2025

Accepted: 29 June 2026

Published online: 10 July 2026

Check for updates

Wenguang Zhao[1,12], Zijian Li[2,12], Mingyang Li[3,4,12], Hengyu Ren[1], Cong Lin[4], Haocong Yi[1], Shengyu Wu[5], Xiaohu Wang[1], Jun Wang[6], Bin Fei[2], Muyu Zhang[7], Mingwei Wang[8], Ye Sun[8], Guojie Chen[1], Zhefeng Chen[1], Weixin Chen[9], Xiaoxu Zhao[8], Shunning Li[1,10] ✉, Dong Zhou[11] ✉, Qinghe Zhao[1,5] ✉ & Feng Pan[1] ✉

Although the anionic activity in layered oxide positive electrodes is partially understood, the mechanism by which it induces internal crack propagation under high-voltage conditions remains unclear, severely limiting stable cycle life and available capacity. In this study, the mechanism underlying internal crack propagation is elucidated in $LiCoO_2$ under harsh float-charge conditions at 60 °C and a potential of 4.6 V vs. Li^+/Li. We reveal that sequential phase transitions from O3 to O1 and then to a cation-mixed phase during deep Li^+ extraction generate significant lattice-mismatch stresses that initiate internal cracks. Crucially, the accompanying anionic activity drives the migration of the oxidized lattice O^{n-} ($0 < n < 2$) towards these cracks, where it even accumulates as molecular O_2 that can be released upon crack propagation to the surface. It is identified that the sustained O1tocation-mixed phase transition and the bulk lattice O^{n-} migration synergistically drive the interior crack propagation, ultimately leading to $LiCoO_2$ disintegration and electrochemical degradation. This work not only deepens our understanding of the anionic activity in layered positive electrodes but also provides mechanistic insights for the future design of stable $LiCoO_2$ positive electrodes.

As a cornerstone positive electrode in commercial lithium-ion batteries (LIBs), layered $LiCoO_2$ (LCO) is extensively applied and dominates portable electronics[1,2]. However, to meet the escalating demand for higher energy density, operating LCO at elevated charge potential above 4.55 V (vs. Li^+/Li) is crucial for accessing its full capacity[3]. This high-voltage operation, however, inherently triggers severe structural instability and causes rapid electrochemical deterioration[3]. Our previous investigations have illuminated that the high-voltage instability is

[1]School of Advanced Materials, Peking University Shenzhen Graduate School, Shenzhen 518055, China. [2]School of Fashion and Textiles, The Hong Kong Polytechnic University, Kowloon, Hong Kong SAR 999077, China. [3]Department of Mechanical and Energy Engineering, Southern University of Science and Technology, Shenzhen 518055, China. [4]Department of Chemistry, The Hong Kong Polytechnic University, Kowloon, Hong Kong SAR 999077, China. [5]College of Physics and Energy, Fujian Normal University, Fujian Provincial Key Laboratory of Quantum Manipulation and New Energy Materials, Fuzhou 350117, China. [6]School of Innovation and Entrepreneurship, Southern University of Science and Technology, Shenzhen 518055, China. [7]Department of Mechanics and Aerospace Engineering, Southern University of Science and Technology, Shenzhen, Guangdong 518055, China. [8]School of Materials Science and Engineering, Peking University, Beijing 100871, China. [9]School of Materials, Sun Yat-sen University Shenzhen Campus, Shenzhen 518107, China. [10]School of Energy and Environment, City University of Hong Kong, Kowloon, Hong Kong SAR 999077, China. [11]School of Advanced Energy, Sun Yat-sen University Shenzhen Campus, Shenzhen 518107, China. [12]These authors contributed equally: Wenguang Zhao, Zijian Li, Mingyang Li. ✉e-mail: lisn@pku.edu.cn; zhoud37@mail.sysu.edu.cn; zhaoqinghe@fjnu.edu.cn; panfeng@pkusz.edu.cn

intricately associated with the surface lattice curvature[4], irreversible phase transitions (e.g., the well-established O3 → H1-3 → O1 pathway)[4,5], and the activation and subsequent release of lattice O^{n-} upon deep delithiation[6,7], which are coupled with cation disordering[8]. These factors collectively contribute to the intrinsic degradation mechanisms of LCO.

Historically, research into LCO degradation at high voltages has predominantly focused on surface structural evolution, often describing a surface-to-bulk degradation pathway[9–11]. This surface-centric view highlights two primary aspects. First, the gradual activation of surface lattice O^{n-} ($0 < n < 2$) leads to the migration and loss of O and Co[12], which subsequently accelerates cation mixing while triggering irreversible phase transitions in the surface regions[13]. As a result, this progressively transforms the LCO surface to spinel and then rock-salt (RS) phases, critically impeding interfacial Li^+ transport, causing heterogeneous charge distribution[14], and ultimately leading to rapid capacity decay[15,16]. Second, electrolyte decomposition, particularly the formation of corrosive species such as HF, further exacerbates surface degradation and destabilizes surface-protective cathode/electrolyte interphase (CEI)[9,17–19]. However, these surface-dominated mechanisms do not adequately explain the bulk structural degradation observed through crack formation. Despite their frequent observation and wide recognition, the precise mechanisms of crack propagation and their localized microscopic origins within LCO bulk remain significantly underexplored.

Upon deep delithiation, layered-oxide positive electrodes are known to undergo complex phase transitions, accompanied by significant anisotropic lattice distortions and accumulation of lattice-mismatch stress. This ultimately leads to the mechanical degradation and microcrack formation within individual particles[2,8,20–22]. Generally, the high-voltage-induced O3-to-O1 phase transition, often proceeding through the H1-3 intermediate, is particularly pronounced, causing localized lattice dislocations and Co-O slab bending. These structural changes further induce drastic lattice variations with Co-O slab slippage, local structure collapse, and even oxygen reorganization[15,23]. As a result, substantial residual strain is accumulated with concentrated tensile and compressive stresses, initiating subsequent internal cracks and further particle fragmentation[24]. Recent studies have also highlighted a strong correlation between lattice strain-induced oxygen vacancies O_V) and reduced barriers for lattice oxygen release, which can intensify crack propagation along the (003) basal planes[25]. However, the precise mechanism by which the anionic activity contributes to the internal crack propagation in LCO upon deep delithiation is largely elusive.

Given the practical significance of developing high-voltage and high-energy-density LIBs, it is imperative to elucidate the mechanisms and critical factors governing the propagation of internal cracks in LCO, a pervasive phenomenon and a major contributor to electrochemical degradation. To this end, we employed float tests[26], a robust accelerated aging technique, to assess the long-term stability related to interior cracks. Here, with various experimental techniques and theoretical calculations, we present the mechanistic study of the interior crack propagation within LCO. By carefully minimizing the influence of external factors (particularly the surface effects and electrolyte degradation), our results reveal a synergistic phase transition and lattice O^{n-} migration-induced crack propagation mechanism. Specifically, upon nearly complete delithiation, the bulk lattice O^{n-} in O1 phase tends to migrate towards interior cracks and accumulates there, forming molecular O_2 trapped inside LCO bulk. This process is concurrently accompanied by the emergence of a cation-mixed (CM) phase. Crucially, the subsequent float charge further exacerbates the internal stress along the O1/CM phase boundaries, significantly promoting the interior crack propagation. Our findings demonstrate that the sustained O1-to-CM phase transitions and the migration of oxidized lattice O^{n-} species, coupled with molecular O_2 accumulation, synergistically drive the continuous propagation of interior cracks that eventually penetrate throughout the particle to the surface, leading to gaseous O_2 release and severe LCO disintegration. With this fundamental mechanism underlying LCO crack propagation, our study may not only deepen understanding of LCO degradation but also provide valuable guidance for the design of advanced layered-oxide positive electrodes.

Results

Phase transition of LCO upon float charge

A commercial LCO, characterized by a large D_{50} value of about 15 μm and containing trace Al (4500 ppm), Mg (1500 ppm), and Ti (500 ppm), was selected for this investigation into the degradation under float conditions. To assess the float-charge performance and induced degradation, coin-type Li||LCO cells were assembled and used. Float charge tests were performed by initially charging the cells to 4.6 V with a constant current (CC) of 100 mA g^{-1} (CC stage), followed by constant voltage (CV) charging at 4.6 V (CV stage) (Fig. 1a). Fundamental characterizations, including scanning electron microscopy (SEM) (Supplementary Fig. 1), X-ray diffraction (XRD) coupled with Rietveld refinement (Supplementary Fig. 2), and transmission electron microscopy (TEM; Supplementary Fig. 3), confirmed a uniformly smooth surface and a pure α-$NaFeO_2$-type layered structure with an *R*-3*m* space group. However, the enlarged image in Supplementary Fig. 3b reveals the presence of unavoidable inherent defects, such as curves in partial Co-O layers within the commercial LCO, which is difficult to eliminate in actual production.

Under the high temperature float charge conditions, progressive crack formation was distinctly observed during float charge from 0 to 40 h (Supplementary Fig. 4). Further investigation into the temperature dependence of this degradation revealed a pronounced increase in leakage current above 50 °C, underscoring the accelerated degradation kinetics at elevated temperatures (Supplementary Fig. 5). Consistent with this, the extent of crack formation varied with temperature: at 25 and 45 °C, only slight cracks appeared, whereas at 60 °C, severe particle disintegration was evident (Supplementary Figs. 6 and 7). To further elucidate the propagation of interior cracks, cross-sectional TEM analyses were conducted on the samples after float charge at 25, 45, and 60 °C for an extended duration of 120 h (Supplementary Fig. 8). These analyses demonstrated that while only minor interior cracks were observed at 25 °C, extensive interior cracking became prevalent with increased temperature.

XRD analysis revealed that, after float charge for 120 h, O1 phase became dominant, a notable deviation from the H1-3 phase typically expected at such a high voltage (Fig. 1b). High-resolution scanning TEM (STEM) combined with geometric phase analysis (GPA) revealed heterogeneous O1 domains embedded within the charged LCO bulk before float charge (Supplementary Fig. 9). As a drastically compressed structure, O1 stacking imposes pronounced stresses on the adjacent O3 matrix. This stress evidently intensifies the curvature of the Co-O layers. To elucidate the correlation between stress evolution and crack propagation under different float charging durations, systematic analyses using 4D STEM were conducted (Supplementary Figs. 10–13). Specifically, the stress distribution mapping and line-scan profiles reveal a pronounced spatial correlation between stress-concentration regions and crack locations, suggesting that localized stresses induced by phase transitions and other factors are a critical driving force for crack propagation. To quantitatively assess the relationship between stress concentration severity and crack geometry, a stress concentration factor *K*, defined as $K = 1 + 2\times(L/W)$, where *L* and *W* denote crack length and width, respectively, was introduced (Supplementary Fig. 14). The results demonstrate a monotonic increase in *K* with prolonged float charging time, rising from 3.37 at 5 h to 7.80 at 20 h, 9.50 at 40 h, and ultimately reaching 20.26 at 120 h, indicating progressively intensified stress concentration. More critically, a

https://doi.org/10.1038/s41467-026-75373-2

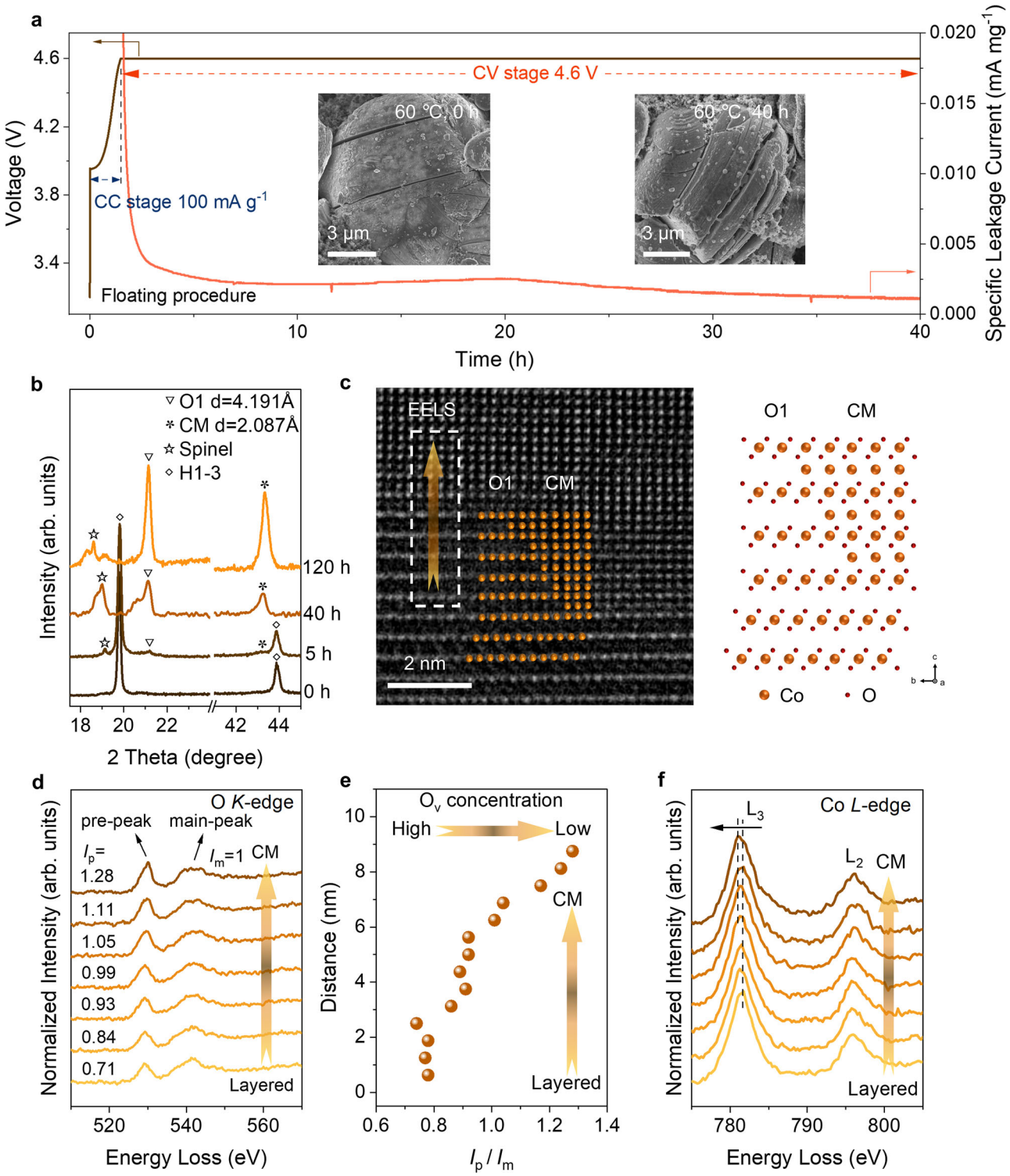


Fig. 1 | Structural evolution during float charge. a Electrochemical charge profile of the Li||LCO cell, with the insets showing the particle morphology after 5 and 40 h of CV stage at 60 °C. **b** Ex situ XRD patterns of LCO after float charge at 60 °C for different durations (0, 5, 40, and 120 h). **c** STEM image of LCO after float charge for 5 h at 60 °C (left) and corresponding structural sequencing models of O1 and CM phases (right), with the yellow arrow indicating the EELS line-scan direction. **d** O *K*-edge EELS spectra collected along the path in **c**, with I_p/I_m labeled for each spectrum. **e** Distribution of O_V derived from (**d**). **f** Co *L*-edge EELS spectra collected along the path in (**c**).

previously unreported phase characterized by a layer spacing (d = 2.087 Å) approximately half that of the O1 phase (d = 4.191 Å) was identified after float charge for 5 h (Supplementary Fig. 15). This newly formed phase, which we term the cation-mixed (CM) phase, originates from Co migration into the Li layer of the O1 phase under certain stress disturbances (such as more curved Co-O layers and more dislocations). Subsequently, driven by the internal stress, lattice oxygen undergoes oxidation and migration. The oxygen vacancies generated during this process, along with the induced local distortions and coordinatively unsaturated sites, significantly lower the energy barrier for Co ions to

hop into adjacent vacancies in the Li layer. Ultimately, under the synergistic driving forces of internal stress, lattice oxygen migration, and vacancies in the Li layer, a portion of Co ions irreversibly migrate from the Co-O layer into the Li layer, thereby forming the structurally disordered CM phase. Aberration-corrected STEM (AC-STEM) confirmed the atomic structure of the CM phase, suggesting that it forms a semi-coherent interface with the O1 phase (Fig. 1c). The occurrence of this CM phase in LCO indicates the increased cation disorder and significant lattice Co and O loss under severe float conditions, a key indicator of bulk degradation[27].

The emergence of the CM phase is not merely a consequence of excessive Li^+ extraction; rather, our findings suggest that the float charge actively facilitates the migration of bulk lattice O^{n-}, which is considered the primary driver for the CM phase formation. This crucial mechanism was further confirmed by electron energy loss spectroscopy (EELS) performed across regions transitioning from the layered to CM phases (Fig. 1d). In the EELS spectra, the pre-edge feature around 530 eV corresponds to the O 1*s* → O 2*p*–Co 3*d* hybridized states, while the main edge at around 541.5 eV is attributed to the core-level O 1*s* → O 2*p* transitions[28]. The intensity ratio of the pre-edge (I_p) to the main edge (I_m), denoted as I_p/I_m, directly correlates with the concentration of O_V[29]. Notably, as shown in Fig. 1e, the O_V concentration was found to decrease upon transition from the layered to the CM phase. This indicates that the substantial oxygen loss from the layered phase drives the generation of under-coordinated Co ions, which then migrate into the Li layers to form the structurally rearranged and potentially more stable CM phase. Concurrently, the Co L_3-edge peak shifts to lower energy in the CM phase, further corroborating a reduction in Co oxidation state (Fig. 1f), a direct consequence of O loss and structural rearrangement within the LCO lattice.

Formation of molecular O_2 trapped in interior cracks

As discussed previously, the formation of the CM phase within LCO induces significant internal stresses at its boundary with the layered phase due to their distinct lattice configurations, which serve as the critical initiation sites for interior cracks. To investigate the origin and propagation of these cracks, particularly those formed after float charge for 5 h, high-resolution STEM coupled with GPA was performed (Fig. 2a–c). Analysis reveals concentrated regions of intense tensile (shown by red) and compressive (shown by green) stress localized at the crack tips, indicating these stresses as the primary driving force for crack propagation (Supplementary Fig. 9). Further structural analysis of the crack-tip region shows the coexistence of layered O1 and CM phases (Supplementary Fig. 15), where the inherent lattice mismatch at their interface acts as the starting point for these internal cracks. Continued float charge under high-voltage conditions further promotes this crack propagation, ultimately leading to severe particle disintegration.

Beyond stress-induced crack initiation, our comprehensive analyses, including EELS, electron paramagnetic resonance (EPR), and in situ differential electrochemical mass spectrometry (DEMS), also elucidate the crucial role of bulk lattice O^{n-} migration in the crack propagation mechanism. Specifically, the O *K*-edge EELS spectra reveal a significant increase in O_V concentration from LCO bulk towards the crack tips (Fig. 2e, f), indicating the substantial loss of bulk lattice O^{n-} at these defect sites. This observation supports our hypothesis that the interior cracks, serving as the in situ-formed defects, provide preferential and shorter diffusion pathways for the O^{n-} migration and, critically, the confined spaces for molecular O_2 accumulation. EPR measurements provide evidence for the presence of molecular O_2 within these interior cracks (Fig. 2g): characteristic resonance signals between 5500 and 9000 G were detected in the LCO after float charge for 10 h[30]. However, the LCO that undergoes float charging at 25 °C does not produce a significant O_2 signal (Supplementary Fig. 16). The release of this trapped molecular O_2 was further probed by in situ DEMS (Fig. 2h and Supplementary Fig. 17). Supplementary Fig. 18 displays the resonant inelastic X-ray scattering (RIXS) spectra comparing pristine LCO with the LCO after float charging at 60 °C and 4.6 V for 10 h and 20 h. The absence of detectable signals in pristine LCO, in stark contrast to the clear RIXS signatures observed for the LCO after 10 h and 20 h of charging, substantiates the formation of O_2 in the LCO bulk. Our findings suggest that the accumulated molecular O_2 within the interior cracks induces additional internal stresses that drive crack propagation, in addition to the lattice-mismatch-induced internal stresses. In addition, DEMS reveals pronounced O_2 evolution between 8 and 20 h of float charge, which coincides with an increase in the float charge capacity (C_{float}) from 10 to 20 h and indicates a close correlation between gaseous O_2 release and C_{float} increase. This underlying correlation can be elucidated as follows. First, as the float charge proceeds, the concentration of oxidized lattice O^{n-} increases, and these O^{n-} ions migrate into the interior cracks and form molecular O_2 there. When these interior cracks propagate sufficiently to reach the particle surface, the trapped O_2 is released, producing the observed surge in O_2 signal. Second, the subsequent propagation of these cracks to the surface exposes fresh and highly active LCO interfaces (with active species like Co^{4+}/O^{n-}) to the electrolyte, which triggers intense interfacial side reactions. These reactions are directly responsible for the observed increase in C_{float}. This precise correlation between O_2 evolution and current response supports the proposed mechanism of high-temperature (HT) floating-induced failure, which originates from bulk oxygen oxidation and crack propagation.

Propagation of interior cracks

To gain a deeper understanding of the dynamic interior crack propagation, transmission X-ray microscopy (TXM) coupled with X-ray absorption near-edge structure (XANES) and extended X-ray absorption fine structure (EXAFS) was further employed (Fig. 3a, b). In TXM images, lighter regions correspond to the lower-valence Co, whereas darker regions indicate the higher-valence Co. After float charge for 5 h, LCO bulk exhibits a uniform distribution of Co valence, suggesting that the overall bulk structure remains largely intact at this early stage. However, a stark contrast emerges after float charge for 40 h, i.e., the Co valence distribution becomes highly heterogeneous, indicating extensive bulk degradation that is attributed to the large-scale migration of lattice O^{n-} and the propagation of interior cracks. Complementary TEM images further corroborate these findings, revealing a pronounced CM phase and intensified crack growth between 5 and 40 h of float charge (Supplementary Fig. 19). This highlights the close correlation between the O1-to-CM phase transition and the propagation of interior cracks. Cross-sectional TEM analyses of the LCOs after float charge for 5, 20, and 40 h further show that the interior cracks preferentially initiate along the (003) planes and subsequently coalesce into larger and more destructive fissures during prolonged float charge (Supplementary Fig. 20). Furthermore, TXM tomography provides a powerful three-dimensional visualization of the internal crack networks (Fig. 3c). Its quantitative analysis shows that the volume fraction of interior cracks dramatically increases from 2.06% to 5.51% between 5 and 40 h of float charge, clearly illustrating the rapid and extensive propagation of these interior cracks.

XANES was also employed to monitor the dynamic changes in lattice O^{n-} migration and local structural evolution (Fig. 3d and Supplementary Fig. 21a). XANES analysis of the Co absorption edge reveals a shift to higher energy after 20 h of float charge, consistent with an increase in Co oxidation state associated with the O3 → O1 phase transition[31]. However, it moves to the opposite direction after further float charge for 120 h, reflecting a decrease in Co valence due to the substantial lattice O^{n-} release, a key event in the degradation process. Further insights into the local structural evolution were enabled by EXAFS analysis (Fig. 3e and Supplementary Fig. 21b). The nearest Co–O coordination shell first shifts to a reduced radial distance after float

https://doi.org/10.1038/s41467-026-75373-2

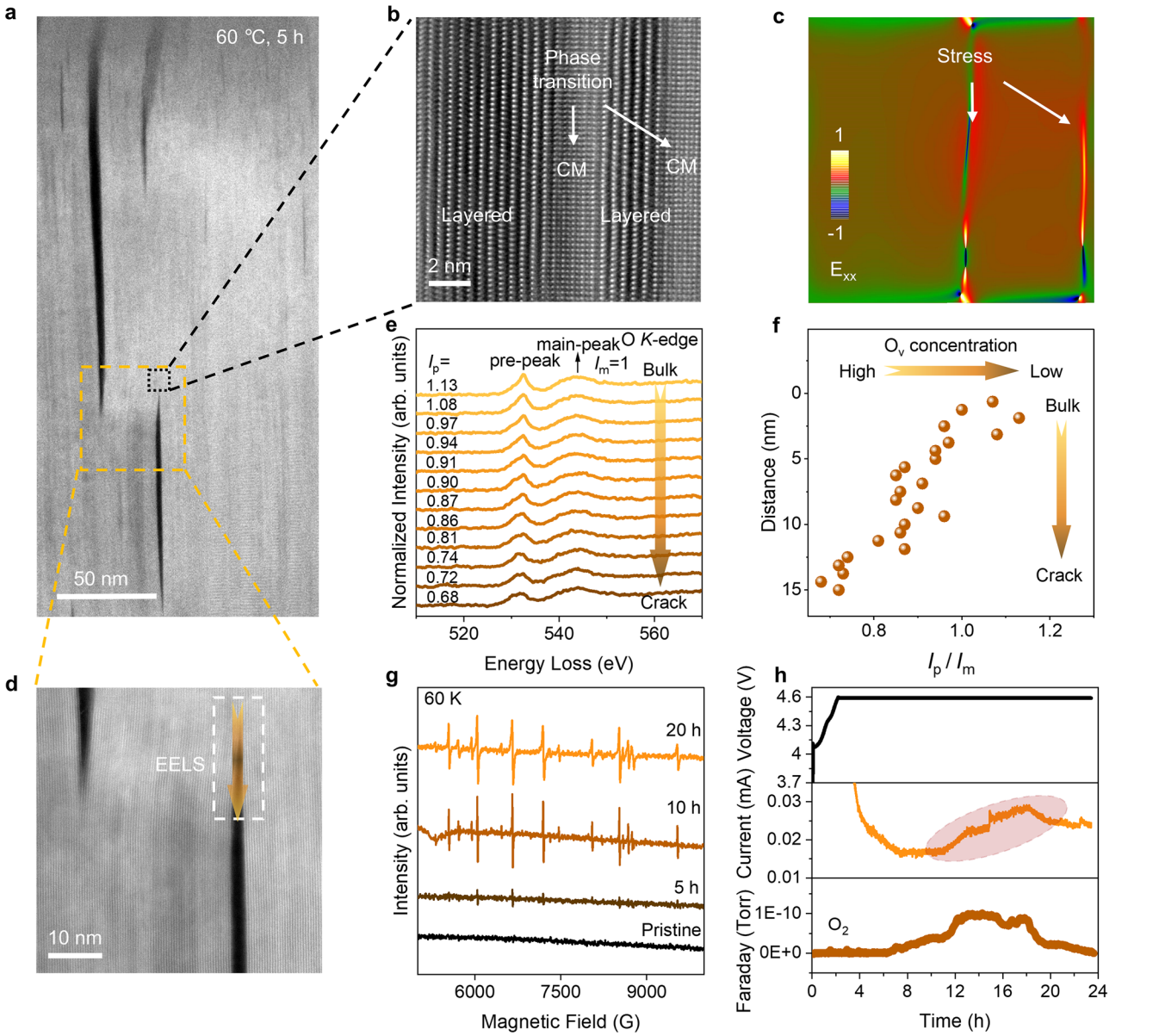


Fig. 2 | Evolution of interior cracks and lattice oxygen during float charge. **a** Cross-sectional STEM image after float charge for 5 h at 60 °C, with the orange box indicating the specific region magnified in (**d**). **b** High-resolution STEM image of the corresponding region at the crack tip in (**a**). **c** GPA map of the corresponding region in (**b**). **d** Enlarged STEM image of the corresponding region in (**a**), with the white box and yellow arrow indicating the respective region and direction of the O *K*-edge EELS spectra. **e** O *K*-edge EELS spectra collected along the path in (**d**). **f** Distribution of O_V derived from (**e**). **g** EPR spectra of LCO after float charge for various durations (5, 10, and 20 h) at 60 K. **h** In situ DEMS profile, with voltage profile (top), leakage current (middle), and corresponding O_2 signal (bottom). An increase in the leakage current is observed after float charge for 10 h.

charge for 20 h, signifying shorter Co–O bond lengths characteristic of the O1 phase[32]. By contrast, it shifts back after 120 h, indicating bond elongation, consistent with the formation of the CM phase. Unlike Co–O, the first Co–Co coordination shell exhibits a sustained decrease in radial distance throughout the float charge process, directly attributed to the transition of O1 to CM phase. Moreover, the diminished peak intensities and contracted distances at higher *R*-values (4–10 Å) for other Co–O and Co–Co coordination shells after float charge for 120 h reveal the widespread existence of structural disorder within LCO.

Theoretical calculations on the migration of bulk lattice O^{n-}

These experimental observations above, including EELS, in situ DEMS, XANES, and EXAFS, clearly illustrate the migration of bulk lattice O^{n-} to the interior cracks in LCO, which is at the core of the proposed mechanism linking molecular O_2 accumulation and crack propagation. To further elucidate the precise underlying atomic-scale mechanisms, theoretical investigations were conducted. Here, we employed Monte Carlo (MC) simulations and percolation theory to evaluate the capability of O^{n-} migration within LCO[33]. Our theoretical model was predicated on the understanding that during the O1-to-CM phase transition, Co migrates from its original CoO_6 octahedron into the interlayer region, leaving behind several types of under-coordinated O ions (i.e., connected with fewer than three Co ions) that tend to be oxidized to O^{n-}. Crucially, these redox-active O^{n-} species can form a continuous migration pathway within the anion sublattice, similar to the case of Li-rich layered-oxide positive electrodes. For computational efficiency, we simplified the anion sublattice into a two-dimensional cellular network representing O^{n-} migration from the bulk to the boundary (Fig. 4a). In these MC simulations, the redox-

https://doi.org/10.1038/s41467-026-75373-2

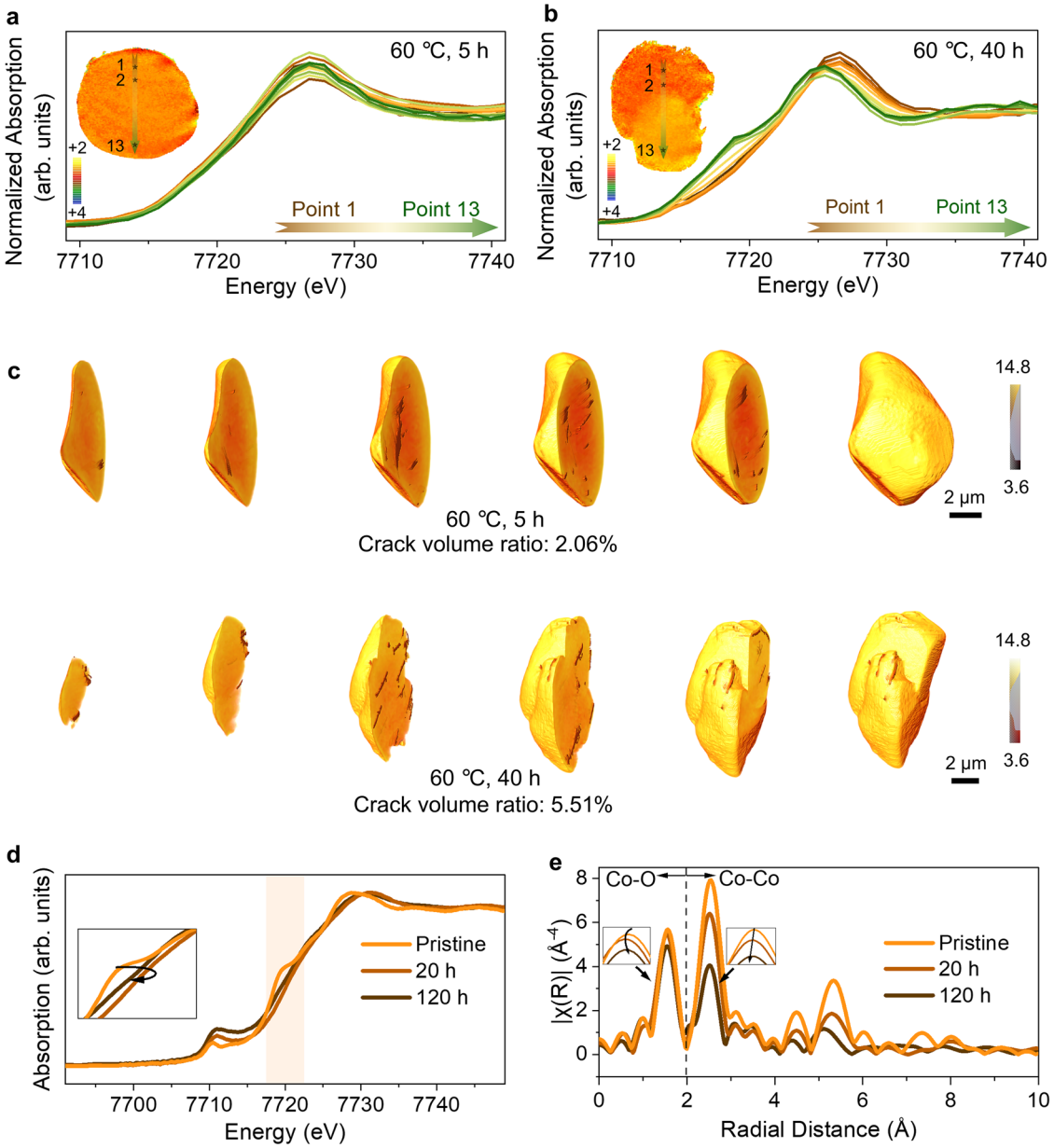


Fig. 3 | Evolution of Co valence and internal cracks during float charge. a, **b** Co *K*-edge XANES spectra of LCO after float charge for 5 (**a**) and 40 h (**b**) at 60 °C, with Co valence distribution from XANES shown as the insets. **c** Three-dimensional visualization of the internal crack networks after float charge for 5 (top) and 40 h (bottom) at 60 °C. The gray level in the histogram increases with the local density, i.e., lower gray values indicate cracks and holes. **d** Co *K*-edge XANES spectra of LCO after float charge for different durations (20 and 120 h) at 60 °C, with the inset showing a magnified view at around the half-maximum of the absorption edge. **e** Corresponding Fourier-transformed k3-weighted EXAFS spectra, with the inset showing a magnified view of the corresponding Co-O and Co-Co peaks.

active lattice O^{n-} species are defined as the under-coordinated O ions induced by Co migration. A migration pathway for lattice O^{n-} is established when two adjacent redox-active O^{n-} sites are connected to the same Co ion, and once the concentration of these redox-active lattice O^{n-} sites reaches a critical threshold, a continuous network for O^{n-} migration emerges.

As the O1-to-CM phase transition progresses, the proportion (denoted as α) of Co migrating to the interlayer region increases. The simulations demonstrate that at the early stages of Co migration ($\alpha < 0.2$), the connection probability (p) of redox-active O^{n-} sites—representing the likelihood of forming a continuous pathway from one boundary to another—remains less than 0.05 (Fig. 4b). However, as α surpasses 0.5, p increases sharply to over 0.9, indicating that nearly the entire network of redox-active O^{n-} sites becomes fully connected to the boundary. This is known as the percolation of redox-active O^{n-} in the anion sublattice, upon which the oxidized lattice O^{n-} can migrate over long distances to the LCO surface or cracks, ultimately leading to the release of gaseous O_2. Significantly, our analysis shows that the distribution of Co ions within the CM phase exactly aligns with the case of $\alpha = 0.5$; that is, half of the Co ions are located in their original layer of the corresponding O1 phase, while the other half occupy the interlayer region. This suggests that before the complete formation of the CM phase, a considerable fraction of redox-active lattice O^{n-} can diffuse to the boundary during the Co migration, thus generating a substantial amount of O_V in the lattice. When α approaches 0.5, the accumulated O_V triggers an atomic rearrangement of the anion sublattice, culminating in the formation of the CM phase, which, as observed experimentally, exhibits a much lower O_V concentration. These results

https://doi.org/10.1038/s41467-026-75373-2

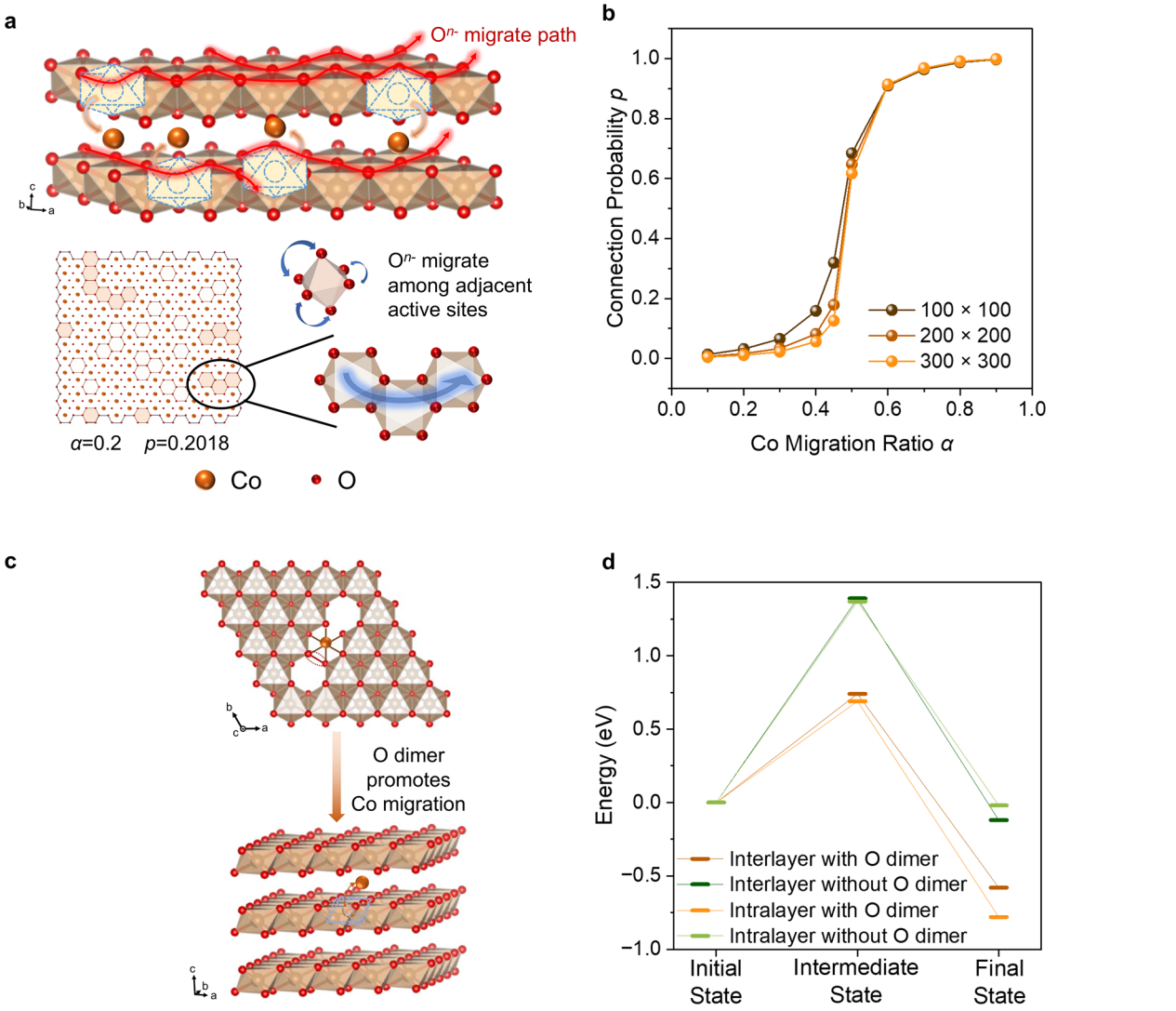


Fig. 4 | Theoretical investigation of the migration of lattice O^{n-} and Co during the O1-to-CM phase transition. a Migration pathway of the redox-active lattice O^{n-} after Co migration to the interlayer region. Note that Co and O atoms are represented by orange and red spheres, respectively. **b** Relationship between Co migration ratio (α) and the connection probability of O^{n-} (p). **c** Schematic illustration of O dimer facilitating Co migration. Note that Co and O atoms are represented by orange and red spheres, respectively. **d** Migration barriers for Co in the presence and absence of bulk O dimer.

suggest that the formation of CM phase and the long-range migration of lattice O^{n-} are mutually synchronized, and this theoretical insight explains our experimental observations that the accumulation of molecular O_2 at the interior cracks is consistently accompanied by the CM phase emergence near the crack tips.

Beyond the above migration pathways, we further studied the atomic-level mechanisms facilitating these transformations using density functional theory calculations within the Hubbard U-corrected generalized gradient approximation (GGA+U). PBE-based methods are known to have limitations in accurately describing correlated electronic states and the relative energies of transition-metal and oxygen states in transition-metal oxides[34,35]. In this context, more advanced approaches, such as dynamical mean-field theory (DMFT) and related beyond density functional theory (DFT) treatments, have been reported in the literature for correlated oxides including Li_xCoO_2[34,36,37]. However, the high computational cost of these methods prevents their application to the large simulation cells considered in this work. Indeed, we have compared the results between GGA + U and the Heyd-Scuseria-Ernzerhof (HSE06) hybrid functional for LCO (Supplementary Figs. 22 and 23), which supports the reliability of GGA + U in capturing the qualitative trends in the electronic structure (e.g., enhanced oxygen activity). Therefore, all the calculations provided below are based on the GGA + U scheme. The formation of O dimers within LCO bulk is considered a prerequisite for generating molecular O_2, yet its mechanistic role in the O1-to-CM phase transition remained unclear. As shown in Fig. 4c, we investigated the scenario where one Co ion migrates near an O dimer formed within the corresponding CoO_6 octahedron in the initial configuration. Both the intralayer and interlayer migrations of Co ions were evaluated. Our calculations demonstrate that the presence of an O dimer significantly reduces the energy barriers by 0.65 and 0.68 eV for intralayer and interlayer Co migration, respectively (Fig. 4d). Even in the presence of some residual Li (with SoC = 90.9%, Supplementary Fig. 24), the formation of an O dimer can still accelerate the Co migration. This finding indicates that the formation of O dimers actively accelerates the Co migration, thereby facilitating the O1-to-CM phase transition. Given the low kinetic barriers in the delithiated O1 phase, the Co migration likely precedes both the long-range migration of lattice O^{n-} and the propagation of interior cracks, which is consistent with the experimentally observed rapid formation of the CM phase within LCO bulk.

https://doi.org/10.1038/s41467-026-75373-2

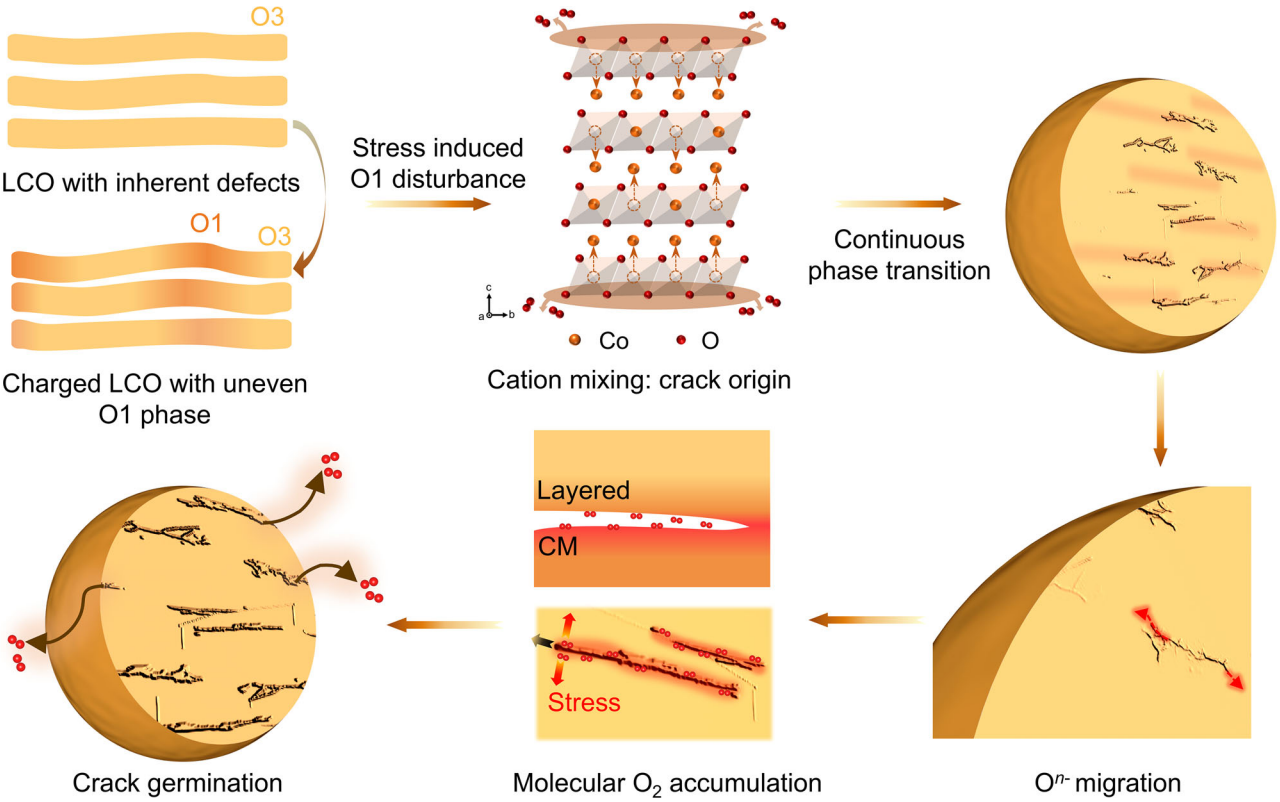


Fig. 5 | Proposed mechanism of interior crack propagation in LCO under float-charge conditions. Starting from LCO containing inherent lattice defects, deep Li^+ extraction triggers the O3-to-O1 phase transition and induces unevenly distributed O1 domains within the charged particles. Stress disturbances around these distorted O1 regions then promote the Co migration into the Li layer, producing a CM phase that serves as the crack origin (Co and O atoms are depicted as orange and red spheres, respectively). The continuous O1-to-CM phase transition further imposes the lattice-mismatch stress at the layered/CM phase boundaries, leading to the interior crack nucleation. Meanwhile, the oxidized lattice O^{n-} migrates along the defect-rich regions toward these nascent cracks and accumulates there as molecular O_2. Such trapped O_2 exerts additional local pressure at the crack tips that, together with the lattice-mismatch stress, expands the cracks and accelerates their propagation. Once the cracks extend to the particle surface, the accumulated O_2 is released, and the newly exposed interfaces undergo intensified side reactions with the electrolyte, ultimately resulting in the severe particle disintegration and electrochemical degradation.

Degradation mechanism

In addition to bulk degradation, we also observed severe surface degradation of LCO under float charge conditions. This pronounced degradation is primarily attributed to two factors. First, an elevated state of charge (SOC) at the LCO surface promotes the generation of highly oxidative Co^{4+} and O^{n-} species. Second, this environment accelerates the electrolyte decomposition, leading to the formation of corrosive species such as HF and HPO_2F_2. Nuclear magnetic resonance (NMR) analysis of the electrolytes cycled at 25, 45, and 60 °C demonstrates the temperature-dependent increase in the characteristic peaks of $PO_2F_2^-$, a byproduct of HF, at chemical shifts of −83.0 and 85.5 ppm (Supplementary Fig. 25). This indicates enhanced formation of HF and HPO_2F_2 and severe SiO_2-based glass corrosion at elevated temperatures. Correspondingly, X-ray photoelectron spectroscopy (XPS) signals of Co on Li negative electrodes from the Li||LCO cells after float charge for 120 h intensify markedly with increased temperature, directly reflecting the accelerated HF-induced Co dissolution from the LCO surface (Supplementary Fig. 26).

At 60 °C, the LCO surface undergoes significant morphological and structural changes. A highly porous surface layer, exceeding 100 nm in thickness, is observed (Supplementary Fig. 27), predominantly as a consequence of the severe Co and O loss. Selected-area electron diffraction (SAED) from this region confirms the coexistence of O3, O1, spinel, and RS phases, alongside a distorted lattice, indicative of numerous vacancies and crystal-plane slippage. Furthermore, cross-sectional STEM further reveals a ~5 nm thick amorphous surface film, underlain by a 5–10 nm RS subsurface layer and a mixed O1/CM/spinel bulk phase (Supplementary Fig. 28). Meanwhile, the CEI exhibits a thick and porous morphology (Supplementary Fig. 29), reflecting aggressive interfacial side reactions. Collectively, these integrated observations demonstrate that float charge at 60 °C induces pronounced surface degradation, driven by intensified interfacial reactions, ultimately leading to extensive Co/O depletion and the formation of a porous layer.

Figure 5 comprehensively illustrates the proposed mechanism of interior crack propagation in LCO, highlighting the synergistic interplay between sustained O3 → O1 → CM phase transitions and the collective lattice O^{n-} migration towards the interior cracks. During float charge, continuous Li^+ extraction from the LCO bulk is accompanied by the emergence of uneven O1 domains, which evolve into the CM phase under exacerbated disturbance, such as stresses from Co-O lattice curves. The CM phase transition is also promoted by oxygen oxidation and migration. Oxidized lattice O^{n-} species migrate into Li-layer sites, thereby significantly lowering the energy barrier for Co migration and driving the irreversible formation of the CM phase. These transitions generate more pronounced internal stresses due to lattice mismatch, contributing to the generation and propagation of the interior cracks along the O1/CM boundaries. Simultaneously, as elucidated in previous sections, lattice O^{n-} migrates towards and accumulates within these interior cracks as molecular O_2. The trapped O_2 generates additional localized gas pressure at the crack tip, which synergizes with the lattice-mismatch-induced stress, creating a

combined driving force that effectively wedges open the crack and accelerates its propagation. Upon propagation to the particle surface, the accumulated O_2 is released, and the newly exposed and highly active interfaces undergo aggressive side reactions with the electrolytes (Supplementary Fig. 30). Thus, the synergy between sustained phase transitions and O^{n-} migration continuously drives crack propagation from the bulk to the surface, culminating in severe LCO disintegration and electrochemical degradation.

As the desire for increased energy density of LCO positive electrodes becomes increasingly urgent in industry, there is a pressing requirement to develop LCO with high floating durability at 4.6 V and 60 °C. Our above results have comprehensively demonstrated the interior crack propagation mechanism of LCO, including the sustained O1-to-CM phase transition, accumulation of molecular O_2 in interior cracks, the propagation of cracks in the bulk region of LCO, and severe surface Co/O loss induced by side reactions. Based on these findings, we propose the following strategies to effectively enhance floating durability. Firstly, suppressing the bulk O1-to-CM phase transition is essential, as it serves as the origin for long-range migration of lattice O^{n-} and subsequent propagation of interior cracks. Secondly, it is crucial to develop advanced electrolytes that remain stable at high temperatures (such as 60 °C), thereby reducing electrolyte decomposition and the formation of corrosive acidic species (e.g., HF), which in turn mitigates surface Co/O loss and interfacial side reactions.

From the perspective of bulk durability, structural modifications, especially doping by heteroatoms like Al, have been validated as feasible approaches to enhance the stability of LCO lattice, while their effects in alleviating both the extensive migration of lattice O^{n-} and the propagation of the interior cracks remain insufficiently explored. To this end, the modified LCO was synthesized by incorporating 8000 ppm Al into the LCO bulk (Al-reinforced LCO), with the detailed synthesis provided in the Supplementary Information. Specifically, due to the strong covalent Al-O bonds, the bulk lattice O^{n-} is more effectively stabilized within the crystal structure, thereby significantly enhancing the bulk stability during float testing. Supplementary Fig. 31 compares the XRD patterns of the Al-reinforced LCO after floating for 120 h. At 25 °C, the H1-3 phase predominates the bulk structure of Al-reinforced LCO, with some O3 phase retained. Even at 60 °C, the bulk structure is still dominated by the H1-3 phase, with only a small amount of O1 phase detected, which contrasts with the bare LCO (Fig. 1b). This indicates that the heavy Al doping can effectively suppress the O1-to-CM phase transition, thereby fundamentally reducing the bulk internal stresses and resulting in the more integrated LCO with fewer cracks (Supplementary Fig. 32). Consequently, compared with commercial LCO, the Al-reinforced LCO exhibits a much lower leakage current without obvious gaseous O_2 release upon floating (Supplementary Figs. 33 and 34).

Discussion

In this work, we provide a comprehensive elucidation of the intricate mechanism governing interior crack propagation in LCO during float charge at 4.6 V with elevated temperatures. Upon float charge, the substantial Li^+ extraction triggers a sequential O3 → O1 → CM phase transition. The critical irreversible O1-to-CM phase transition plays a dual role in LCO degradation: it not only generates significant internal stresses that concentrate near the interior crack tips, but also actively promotes the long-range migration of bulk lattice O^{n-}, which in turn leads to the accumulation of molecular O_2 within these interior cracks. The synergistic interplay among these factors, including intensified internal stresses from lattice mismatch at the O1/CM interface and accumulated molecular O_2 within interior cracks, is the primary driving force for crack propagation. As these cracks propagate to the surface, the trapped molecular O_2 is released as gas. Such cascading processes ultimately lead to severe LCO disintegration with pronounced Co and O depletion, further exacerbated by aggressive surface side reactions occurring along the newly exposed crack surfaces. Overall, our study highlights the critical and interconnected roles of the O1-to-CM phase transition and the long-range lattice O^{n-} migration in the interior crack propagation of LCO, providing mechanistic insights into the rational design for advanced layered positive electrodes like LCO with enhanced bulk stability and long-term durability.

Methods

Material characterization

The commercial LCO used in this work was purchased from Pulead Technology Industry Co., Ltd. The XRD was performed on a Bruker D8 Advance diffractometer with Cu Kα radiation (λ = 0.154 nm), and Rietveld refinements of XRD patterns were carried out using the FULLPROF software. Sample morphology and elemental distribution were examined using SEM (Zeiss SUPRA-55) with energy-dispersive X-ray spectroscopy (EDS; Oxford X-Max 80). The CEI was characterized by cryogenic TEM (cryo-TEM): charged electrode powders were harvested by gently scraping the cycled electrode surface with a micro-spatula inside an Ar-filled glovebox. These powders were then dry-dispersed onto the copper grids via direct contact and gentle manual agitation, utilizing physical adhesion to load the sample. This solvent-free approach was chosen to avoid potential dissolution or structural alteration of the CEI caused by organic solvents. The copper grid was then mounted on a Fischione 2550 cryo-transfer holder, and transferred into a field-emission TEM (JEOL JEM-3200FS). The TEM operated at 300 kV, with an emission current of 112 μA. The sample was not exposed to the ambient atmosphere throughout the entire transfer process. High-resolution STEM images and EELS analysis were performed by the double aberration-corrected FEI Titan Themis G2 equipped with a Gatan GIF Quantum ERS spectrometer. The STEM operated at 300 kV, with a beam current of 40 pA. The intensities of the EELS spectra were normalized to ensure consistency across measurements. Specifically, the O *K*-edge spectra were normalized relative to the maximum intensity of the main peak, while the Co *L*-edge spectra were normalized to the maximum intensity of the L_3 peak. Lattice strain fields were analyzed using GPA based on high-resolution STEM images. TEM samples were prepared using the focused ion beam microscope (FIB, Thermo Fisher SCIOS). In situ DEMS measurements employed an EL-CELL EC-DEMS cell, utilizing a perforated coin cell case for the positive electrode to facilitate gas transport. A glass fiber separator was used to ensure high electrolyte wettability and gas permeability. The cell was connected to an online mass spectrometer (Hiden Analytical, HPR-20 EGA). High-purity Ar was used as the carrier gas with a precise flow rate of 0.75 standard cubic centimeters per minute (sccm). After assembly, the cell was allowed to rest for 30 min to reach equilibrium before testing. The electrochemical protocol consisted of a galvanostatic charge/discharge at 100 mA g^{-1}, corresponding to 0.5 C based on 1 C = 200 mA g^{-1}, followed by a float charge (constant voltage) step. To maintain a stable testing environment, the cell mold was heated using a custom-made heating jacket. XPS was carried out on a Thermo Fisher ESCALAB 250Xi using a monochromatic Al Kα X-ray source. The binding energy scale was calibrated by the C 1*s* peak at 284.8 eV. XANES and EXAFS spectra were collected on an easyXAFS300$^+$ spectrometer. The Co *K*-edge XANES spectra were processed using standard procedures. The background was removed by subtracting a linear pre-edge function, and the spectra were subsequently normalized to the average absorption intensity of the post-edge region (edge-jump normalization). TXM tomography data were acquired at the 3D nano imaging beamline (BL18B) of the Shanghai Synchrotron Radiation Facility (SSRF). To ensure reproducibility, a specialized micro-loading procedure was employed. Individual electrode particles were harvested and delivered onto the tip of a micron-tapered glass capillary using an industrial dispenser and a micro-manipulator within an Ar-filled glovebox. To maintain the sample's pristine state and prevent air exposure, the glass capillary was

subsequently encapsulated within a secondary glass tube and sealed. For the TXM-XANES analysis, a pixel-wise normalization procedure was automatically applied to the XANES spectrum of each individual pixel. The normalization was performed by conducting linear regressions on both the pre-edge and post-edge regions. ^{19}F NMR spectra were recorded on a Quantum-Plus 400 MHz spectrometer at 298 K. EPR was performed on a Bruker EMX plus 10/12 instrument equipped with a dual-mode cavity and cooled by an Oxford ESR910 liquid-helium cryostat, and the spectra were recorded in the perpendicular mode at 60 K, with the microwave frequency, power, and modulation amplitude set to 9.645 GHz, 2 mW, and 2 G, respectively[38]. The 4D STEM experiments were conducted on a JEOL JEM-ARM300F2 transmission electron microscope operated at 300 kV, with a beam current of 31 pA and a probe-forming aperture with a 1.3 mrad convergence semi-angle. A Medipix3RX MerlinEM direct electron pixelated detector was employed to capture the 4D STEM dataset. Strain mapping was performed using Python code with reference to the py4DSTEM project[34]. O *K*-edge RIXS measurements were carried out on the U41-PEAXIS beamline of the BESSY II at Helmholtz-Zentrum Berlin (HZB). To avoid air exposure, the samples were sealed in a vacuum suitcase for transfer from an Ar-filled glovebox directly into the measurement chamber. With the scattering geometry fixed at a 60° specular configuration, the energy resolution was calibrated to 90 meV against a carbon-tape reference. Each spectrum was then recorded at an incident photon energy of 531.0 eV over an acquisition window of 30 min[35].

Electrode preparation and electrochemical methods

The positive electrodes were fabricated by mixing LCO (90 wt%), polyvinylidene fluoride (PVDF, 5 wt%) (Aladdin, K30), and acetylene black (5 wt%) (C45 conductive carbon black, TIMCAL) in N-methyl-2-pyrrolidone (NMP) (Aladdin, 99.5%) solvent, followed by casting the slurry onto a 40-μm-thick aluminum foil via coating machine from MTI, Shenzhen Kejing Company (single-side coated) and dried at 120 °C in vacuum for 12 h. The dried electrode sheet was cut into circular pieces of diameter 12 mm via a cutting machine from MTI, Shenzhen Kejing Company. The mass loadings of active materials in the positive electrode films were ~6 mg cm^{-2}. The electrochemical performance was assessed by coin-type (CR2032, i.e., 20 mm in diameter, 3.2 mm in thickness, with the battery casing and the spring made of stainless steel) half cells using Li as the negative electrode (China Energy Lithium Co., Ltd., with 16 mm in diameter, 0.6 mm in thickness, and 99.9% in purity, which was stored in the Ar-filled glovebox for no more than 3 months), Celgard 2400 polypropylene (PP, 25 μm in thickness, 19 mm in dimension, 41% in porosity, 100 ~ 200 nm in pore size) membrane as the separator, 1.0 M $LiPF_6$ in ethylene carbonate (EC) / ethyl methyl carbonate (EMC) / fluoroethylene carbonate (FEC) with a volume ratio of 1:1:1 as the electrolyte (Guangzhou Tinci Materials Technology Co., Ltd.). The volume of the electrolyte for each coin-cell was 60 μL. The float charge measurements were carried out using a NEWARE battery test system at 25, 45, 50, 55, and 60 °C in NEWARE incubator (all batteries were left to rest at 25 °C for 8 hours before cycling). In the float charge procedure, the Li||LCO cells were firstly charged to 4.6 V upon a constant current (0.5 C, 1 C = 200 mA g^{-1}), and then the cells were continuously held at a constant 4.6 V voltage for 120 h. After the float charge, the coin cells were disassembled inside an Ar-filled glovebox (H_2O < 0.01 ppm, O_2 < 0.01 ppm) using a battery disassembling tool (MTI, Shenzhen Kejing Company). The harvested positive electrodes were rinsed twice with anhydrous EMC via manual agitation for 30 seconds each time to remove residual electrolyte salts and then left to dry naturally in the glovebox environment. For SEM, FIB, and XRD measurements, the dried electrodes were mounted onto the holders within the glovebox and experienced only brief exposure to air during the loading process into the equipment chambers. In contrast, for TEM, STEM, XPS, EPR, TXM, CT, and NMR, the samples were loaded into specialized air-tight transfer vessels or sealed tubes inside the glovebox. These containers were only opened within the vacuum chambers or inert environments of the respective instruments to strictly prevent direct contact with atmospheric moisture and oxygen.

Theoretical calculation methods

First-principles calculations were performed within the density functional theory (DFT) framework using the Vienna Ab initio Simulation Package (VASP 5.4.4). Core–valence interactions were treated using the projector-augmented-wave (PAW) method, while exchange and correlation interactions were described using the Perdew–Burke–Ernzerhof (PBE) functional within the generalized gradient approximation (GGA). A kinetic energy cutoff of 500 eV was adopted. Electronic self-consistent convergence criterion was set to 10^{-6} eV, and structural relaxations were carried out until the residual forces on all ions fell below 10^{-4} eV Å^{-1}. The Brillouin zone was sampled using Γ-centered Monkhorst–Pack grids with a minimum k-point density of 0.2 Å^{-1}. To accurately account for the strong on-site Coulomb repulsion of the localized Co 3*d* electrons, a Hubbard correction was applied with an effective U_{eff} of 5.0 eV for Co[36]. Long-range dispersion was incorporated through the semi-empirical DFT-D3 scheme during relaxation. Ionic migration barriers were calculated via the climbing-image nudged elastic band (CI-NEB) method. Detailed calculation parameters and optimized structures are provided in Supplementary Data 1–3. The connectivity of the redox-active lattice O^{n-} was assessed using a Monte Carlo (MC) sampling-based percolation analysis[33]. Given the kinetically prohibitive inter-layer transport of O^{n-} between adjacent Co–O slabs, the analysis was confined to a single slab mapped onto a two-dimensional honeycomb lattice, where each hexagon corresponds to one site. Lattice dimensions of 100 × 100, 200 × 200, and 300 × 300 were tested to ensure finite-size convergence. An oxygen site was defined as redox-active if fewer than three of its nearest-neighbor cation sites were occupied by Co. Two redox-active oxygen sites were considered connected only if they shared a common Co neighbor, allowing the nearest-neighbor segments bridging vacancy-adjacent oxygen to form a continuous pathway. A configuration was defined as percolating when a contiguous network of these redox-active sites spanned the periodic boundaries of the simulation cell. Each MC realization was initialized with a fully Co-occupied slab, followed by the stochastic introduction of Co vacancies until a target concentration (ranging from 0.1 to 0.9) was reached, which mimics the cross-layer Co migration during the phase transition. For each configuration, the percolation probability *p* was calculated as the fraction of redox-active oxygen atoms belonging to a successfully percolating network relative to the total number of redox-active oxygen atoms. To guarantee statistical convergence, *p* was averaged over 10,000 independent random Co vacancy distributions for each degree of cross-layer Co migration.

Data availability

The data generated in this study are provided in the Article, Supplementary Information, Supplementary Data files and Source Data. The optimized computational structures and calculation-related configuration files are provided in Supplementary Data 1–3. Additional data supporting the findings of this study are available from the corresponding authors upon request. Source data are provided with this paper.

References

1. Lv, L. et al. Additive engineering enables aggressive high-voltage $LiCoO_2$ lithium-ion batteries. *Joule* **9**, 101846 (2025).
2. Lyu, Y. et al. An overview on the advances of $LiCoO_2$ cathodes for lithium-ion batteries. *Adv. Energy Mater.* **11**, 2000982 (2021).

3. Konar, R., Maiti, S., Shpigel, N. & Aurbach, D. Reviewing failure mechanisms and modification strategies in stabilizing high-voltage $LiCoO_2$ cathodes beyond 4.55. *V. Energy Storage Mater.* **63**, 103001 (2023).
4. Li, J. et al. Structural origin of the high-voltage instability of lithium cobalt oxide. *Nat. Nanotechnol.* **16**, 599–605 (2021).
5. Lin, C. et al. Structural understanding for high-voltage stabilization of lithium cobalt oxide. *Adv. Mater.* **36**, 2307404 (2024).
6. Ding, W. et al. Tuning surface rock-salt layer as effective O capture for enhanced structure durability of $LiCoO_2$ at 4.65 V. *Adv. Energy Mater.* **14**, 2303926 (2024).
7. Zhao, W. et al. Stabilizing surface lattice O^{n-} (0 <n <2) for long-term durability of LiCoO2. *Angew. Chem. Int. Ed.* **64**, e202503100 (2025).
8. Huang, W. et al. Mechanochemically robust $LiCoO_2$ with ultrahigh capacity and prolonged cyclability. *Adv. Mater.* **36**, e2405519 (2024).
9. Sun, Z., Zhao, J., Zhu, M. & Liu, J. Critical problems and modification strategies of realizing high-voltage $LiCoO_2$ cathode from electrolyte engineering. *Adv. Energy Mater.* **14**, 2303498 (2024).
10. Chen, J. et al. Structure/interface coupling effect for high-voltage $LiCoO_2$ cathodes. *Adv. Mater.* **34**, 2204845 (2022).
11. Zhang, S.-D. et al. Surface engineering of $LiCoO_2$ by a multifunctional nanoshell for stable 4.6 V electrochemical performance. *Energy Storage Mater.* **57**, 289–298 (2023).
12. Cai, M. et al. Stalling oxygen evolution in high-voltage cathodes by lanthurization. *Nat. Energy* **8**, 159–168 (2023).
13. Wang, X. et al. Tuning surface chemistry to reduce the step-like degradation of $LiCoO_2$ at 4.6 V. *Nano Energy* **125**, 109537 (2024).
14. Qian, J. et al. Electrochemical surface passivation of $LiCoO_2$ particles at ultrahigh voltage and its applications in lithium-based batteries. *Nat. Commun.* **9**, 4918 (2018).
15. Li, Z. et al. Revealing the accelerated capacity decay of a high-voltage $LiCoO_2$ upon harsh charging procedure. *Adv. Funct. Mater.* **34**, 2312837 (2023).
16. Zhang, C. et al. Quenching-etched surface spinel to passivate layered cathode materials from structural degradation at high potentials. *Chem. Mater.* **35**, 6692–6701 (2023).
17. Li, W. et al. Understanding and design of cathode–electrolyte interphase in high-voltage lithium–metal batteries. *Adv. Funct. Mater.* **34**, 2406770 (2024).
18. Li, W. et al. Dynamic behaviour of interphases and its implication on high-energy-density cathode materials in lithium-ion batteries. *Nat. Commun.* **8**, 14589 (2017).
19. Liu, M. et al. Hydrolysis of $LiPF_6$-containing electrolyte at high voltage. *ACS Energy Lett.* **6**, 2096–2102 (2021).
20. Lim, J. et al. Intrinsic origins of crack generation in Ni-rich $LiNi_{0.8}Co_{0.1}Mn_{0.1}O_2$ layered oxide cathode material. *Sci. Rep.* **7**, 39669 (2017).
21. Jiang, Y., Qin, C., Yan, P. & Sui, M. Origins of capacity and voltage fading of $LiCoO_2$ upon high voltage cycling. *J. Mater. Chem. A* **7**, 20824–20831 (2019).
22. Hitt, A. et al. Nanotomographic observation and statistical analysis of overcharging induced cracks in $LiCoO_2$ single crystalline particles. *Energy Storage Mater.* **52**, 320–328 (2022).
23. Hu, E. et al. Oxygen-redox reactions in $LiCoO_2$ cathode without O-O bonding during charge-discharge. *Joule* **5**, 720–736 (2021).
24. Lin, W. et al. New insight into bulk structural degradation of high-voltage $LiCoO_2$ at 4.55 V. *Nano Lett.* **24**, 7150–7157 (2024).
25. Morzy, J. et al. Origins and importance of intragranular cracking in layered lithium transition metal oxide cathodes. *ACS Appl. Energy Mater.* **7**, 3945–3956 (2024).
26. Hirooka, M. et al. Degradation mechanism of $LiCoO_2$ under float charge conditions and high temperatures. *Electrochim. Acta* **320**, 134596 (2019).
27. Hirooka, M. et al. Improvement of float charge durability for $LiCoO_2$ electrodes under high voltage and storage temperature by suppressing O1-phase transition. *J. Power Sources* **463**, 228127 (2020).
28. Meng, M. et al. Three dimensional band-filling control of complex oxides triggered by interfacial electron transfer. *Nat. Commun.* **12**, 2447 (2021).
29. Sun, L. et al. Unraveling and suppressing the voltage decay of high-capacity cathode materials for sodium-ion batteries. *Energy Environ. Sci.* **17**, 210–218 (2024).
30. Zhao, C. et al. Coexistence of $(O_2)^{n-}$ and trapped molecular O_2 as the oxidized species in P2-type sodium 3d layered oxide and stable interface enabled by highly fluorinated electrolyte. *J. Am. Chem. Soc.* **143**, 18652–18664 (2021).
31. Park, S. et al. Morphological heterogeneity impact of film solid-state cathode on utilization and fracture dynamics. *ACS Nano* **19**, 21878–21890 (2025).
32. Lin, W. et al. Unraveling atomic-level mechanisms of structural transitions in lithium cobalt oxide under high-voltage conditions. *J. Am. Chem. Soc.* **147**, 16038–16046 (2025).
33. Chen, Z. et al. Influence of Li content on the topological inhibition of oxygen loss in Li-rich cathode materials. *Adv. Mater.* **36**, 2403307 (2024).
34. Banerjee, H. & Morris, A. Theoretical approaches to study degradation in Li-ion battery cathodes: Crucial role of exchange and correlation. *J. Mater. Res.* **40**, 2–35 (2025).
35. Seo, D.-H., Urban, A. & Ceder, G. Calibrating transition-metal energy levels and oxygen bands in first-principles calculations: Accurate prediction of redox potentials and charge transfer in lithium transition-metal oxides. *Phys. Rev. B* **92**, 115118 (2015).
36. Isaacs, E. & Marianetti, C. Compositional phase stability of correlated electron materials within DFT+DMFT. *Phys. Rev. B* **102**, 045146 (2020).
37. Marianetti, C., Kotliar, G. & Ceder, G. A first-order mott transition in Li_xCoO_2. *Nat. Mater.* **3**, 627–631 (2004).
38. Yang, X. et al. Binary eutectic fluoride salts modification enhancing structural stability of layered oxide cathodes for Na-ion batteries. *Energy Storage Mater.* **76**, 104158 (2025).

Acknowledgements

The authors are grateful for assistance from the Steady High Magnetic Field Facilities of the High Magnetic Field Laboratory (Chinese Academy of Sciences) for the EPR measurements, as well as support from SSRF BL18B for the TXM measurements.

Author contributions

F.P., Q.Z., D.Z. and S.L. conceived the work and designed the experiments. W.Z., Z.L. and M.L. carried out the electrochemical measurements. W.Z. and Z.L. carried out the SEM, FIB, TEM, and XRD characterizations, and M.L., H.Y., H.R. and X.W. assisted with the data analysis. H.R. and X.W. performed the DEMS measurement. W.Z., Z.L. and G.C. carried out the EPR, XANES, EXAFS, and TXM characterizations, M.Z., M.W., Y.S. and X.Z. carried out the 4D STEM characterizations, and M.L., S.W., J.W. and B.F. assisted with the data analysis. M.L., Z.C. and W.C. carried out the theoretical calculation, and W.Z., Z.L., C.L. and S. L. assisted with the result analysis. W.Z., Z.L. and M. L. wrote the manuscript, and F.P., Q.Z., D.Z. and S.L. assisted with the manuscript revision. All authors reviewed and approved the manuscript.

Funding

P.F. discloses support for the research of this work from the National Natural Science Foundation of China (Grant No. 92472206), the National Center for International Research of Electric Vehicle Power Batteries and Materials (Grant No. 2015B01015), the Guangdong Key Laboratory of Design and Calculation of New Energy Materials (Grant No. 2017B030301013), the Shenzhen Key Laboratory of New Energy

Resources Genome Preparation and Testing (Grant No. ZDSYS201707281026184), and the Major Science and Technology Infrastructure Project of the Material Genome Big-science Facilities Platform supported by the Municipal Development and Reform Commission of Shenzhen.

Competing interests
The authors declare no competing interests.

Additional information
Supplementary information The online version contains supplementary material available at https://doi.org/10.1038/s41467-026-75373-2.

Correspondence and requests for materials should be addressed to Shunning Li, Dong Zhou, Qinghe Zhao or Feng Pan.

Peer review information *Nature Communications* thanks the anonymous reviewers for their contribution to the peer review of this work. A peer review file is available.

Reprints and permissions information is available at http://www.nature.com/reprints

Publisher's note Springer Nature remains neutral with regard to jurisdictional claims in published maps and institutional affiliations.

Open Access This article is licensed under a Creative Commons Attribution-NonCommercial-NoDerivatives 4.0 International License, which permits any non-commercial use, sharing, distribution and reproduction in any medium or format, as long as you give appropriate credit to the original author(s) and the source, provide a link to the Creative Commons licence, and indicate if you modified the licensed material. You do not have permission under this licence to share adapted material derived from this article or parts of it. The images or other third party material in this article are included in the article's Creative Commons licence, unless indicated otherwise in a credit line to the material. If material is not included in the article's Creative Commons licence and your intended use is not permitted by statutory regulation or exceeds the permitted use, you will need to obtain permission directly from the copyright holder. To view a copy of this licence, visit http://creativecommons.org/licenses/by-nc-nd/4.0/.

© The Author(s) 2026